Energy Advances

PAPER

Check for updates

Interfacing NiV layered double hydroxide with sulphur-doped g-C₃N₄ as a novel electrocatalyst for enhanced hydrogen evolution reaction through Volmer–Heyrovský mechanism†

G. Srividhya, C. Viswanathan (iD) and N. Ponpandian (iD) *

The exploration of non-noble-metal-based catalysts for the hydrogen evolution reaction (HER) is important for the green synthesis of hydrogen *via* electrochemical water splitting. Graphitic carbon nitride (g-C₃N₄) is a widely studied photocatalyst for the HER; however, its intrinsic catalytic activity is poor. In the present study, bare and S-doped g-C₃N₄ were combined with the less explored NiV layered double hydroxide (LDH) and their performance for electrochemical HER catalysis was studied. The fused layers of the composites result in a higher specific surface area and expose a higher number of active centres for better catalytic activity. The composite of sulphur-doped g-C₃N₄ and the NiV LDH showed the least overpotential in comparison with its counterparts, with commendable stability during continuous operation for 8 h. The kinetics of the HER are enhanced by compositing g-C₃N₄ with the NiV LDH, as indicated by the Tafel slope of 79 mV dec^{-1} and impedance spectroscopy analysis. This study proposes a novel g-C₃N₄/NiV LDH-based composite for the HER and gives a comprehensive analysis of the catalytic mechanism in the prepared catalysts.

1. Introduction

Hydrogen energy is a favourable, renewable, and carbon-free solution to the burgeoning energy and environmental crises.[1,2] The sustainable production of hydrogen is obligatory for developing hydrogen energy, where electrochemical hydrogen production from water splitting comes as an efficient and environmental friendly solution.[3,4] Water splitting occurs *via* two half-cell reactions, the hydrogen evolution reaction (HER) and the oxygen evolution reaction (OER), which require noble metals (Pt, Ir) and their oxides (IrO₂, RuO₂), respectively, as electrocatalysts to propel the reactions and reduce the associated overpotential.[5] The cost and rarity of these noble-metal-based catalysts reduces the economic viability of electrochemical water splitting, and hence, HER and OER catalysts based on Earth-abundant materials are being studied extensively by electrochemists worldwide.[6–10]

The HER is the cathodic half-cell reaction in water splitting, and in acidic media, it occurs *via* a two-step process: (i) the adsorption of H$^+$ ions on the catalyst surface to from H*, which is called the Volmer step; and (ii) the second step, which can be either the recombination of adsorbed H* with another solvated H$^+$ to from a H₂ molecule, which is called the Heyrovský step (electrochemical desorption), or the chemical desorption of two H* to form a H₂ molecule, which is known as the Tafel step.[11] Hence, an efficient catalyst should possess enough adsorption sites for the solvated protons and suitable catalytic activity to carry out the second step of either recombination or desorption.[12,13] Moreover, it should good possess structural stability to enable prolonged activity during practical operation. For HER catalysis, it is therefore imperative to design non-noble-metal-based, affordable catalysts with the above-discussed properties.

Graphitic carbon nitride (g-C₃N₄) is a polymeric material and is among the prominently studied metal-free two-dimensional (2D) materials for the photocatalytic and electrochemical production of hydrogen, owing to its high N content.[14] It possesses a graphene-like structure with sp² hybridization of alternate C–N bonds and shows exceptional structural stability, and the vacancy defects around the nitrogen atoms act as catalytic sites for the HER.[15] In addition, it shows a suitable and tuneable band gap for photo-absorption, as well as band edges for photo-electrochemical water splitting, which is advantageous for the direct harvesting of solar energy as chemical energy.[16] However, its high resistance hinders its catalytic performance, and frequent agglomeration of its layered structure blocks the active sites.[17] This can be alleviated

Department of Nanoscience and Technology, Bharathiar University, Coimbatore 641 046, India. E-mail: ponpandian@buc.edu.in; Tel: +91-422-2428423

† Electronic supplementary information (ESI) available. See DOI: https://doi.org/10.1039/d3ya00287j

by different techniques, such as heteroatom doping, hetero-junction engineering, and combining it with other nano-structures.[18–20] Heteroatom doping with phosphorus (P) or sulphur (S) can augment the catalytic activity of g-C$_3$N$_4$ by enhancing the charge transfer kinetics and increasing the number of active sites.[21–23]

Composites of g-C$_3$N$_4$ with transition metal-based materials can drastically increase the catalytic functionality of g-C$_3$N$_4$ due to the intrinsic catalytic activity of transition metals (Ni, Fe, Co, Mn, V, *etc.*).[24,25] Transition metal-based layered double hydroxides (LDHs) are layered ionic compounds made of a positive brucite-like layer, with interlayers of compensating anions and solvent molecules.[26] Since the layered structure exposes more catalytic active sites, they exhibit excellent activity towards water electrolysis.[27,28] In particular, nickel (Ni)-based LDH shows a near-noble-metal catalytic performance for water splitting.[29–31] NiV LDH is a recent addition to the Ni-based LDHs and exhibits exemplary activity towards catalysis of both the HER and OER, owing to its high conductivity along with its layered structure.[32]

Recent studies have suggested that composites based on g-C$_3$N$_4$ and LDHs provide multifunctional activity for photochemical and electrochemical HER and OER processes as well as dye degradation. The Ni–Mn LDH/g-C$_3$N$_4$ nanocomposite has shown effective HER and OER activities, at overpotentials of 147 mV at 60 mA cm^{-2} for the HER and 316 mV at 10 mA cm^{-2} for the OER, along with visible-light degradation activity for the rhodamine B dye.[33] The CoMn LDH@g-C$_3$N$_4$ composite showed a hydrogen evolution current of 50 mA cm^{-2} at an overpotential of 448 mV in 1 M KOH, which is comparable to Pt/C that delivered the same current density at 416 mV.[34] The Mo$_2$C@g-C$_3$N$_4$@NiMn-LDH tertiary composite showed functional activity towards the HER and the OER in an alkaline medium, with respective overpotentials of 116 mV and 298 mV at 10 mA cm^{-2}.[35] Based on these reports, a composite between NiV LDH, which has high conductivity and high catalytic activity, and g-C$_3$N$_4$ may significantly improve the catalytic activity of g-C$_3$N$_4$. For photocatalytic and photoelectrochemical water splitting, most studies on g-C$_3$N$_4$ have focused on band-gap modification *via* heterojunction formation. However, for either electrochemical or photoelectrochemical operation, it is equally important to tune the intrinsic activity, for efficient HER and water-splitting reactions.

In the present work, the electrocatalytic activity of g-C$_3$N$_4$ was improved by doping with S and forming a composite with NiV LDH. Composites of pure and S-doped g-C$_3$N$_4$ with the NiV LDH were prepared and their acidic HER catalysis was studied for the first time. Thin-layered g-C$_3$N$_4$ (gCN) and S-doped g-C$_3$N$_4$ (S-gCN) were prepared through a simple precursor modification, without the need for etching in harsh acids. These layered gCN and S-gCN samples were combined with NiV LDH and their respective physico-chemical and electrochemical HER catalytic properties were studied in an acidic medium, for the first time. Among the prepared samples, S-gCN/NiV showed a minimum overpotential of 560 mV at a current density of 10 mA cm^{-2}, and a Tafel slope value of 79 mV dec^{-1}. This study

reveals that the HER is promoted in the gCN/NiV and S-gCN/NiV catalysts through the Volmer–Heyrovský mechanism, where the strong adsorption of H$^+$ (*i.e.*, the Volmer step) is subdued by the activity of the fused composite layers. The S-gCN/NiV composite catalyst also showed remarkable stability for sustained catalysis up to 8 h. Our study implies that the S-gCN/NiV composite shows a noteworthy HER catalytic activity, benefitting from heteroatom doping and interfacing layered structures, and shows promise as a photo-electrode for the HER.

2. Experimental

2.1 Materials and reagents

All reagents were used as procured without any purification. Melamine (C$_3$H$_6$N$_6$), urea (CH$_4$N$_2$O), thiourea (CH$_4$N$_2$S), nickel(ɪɪ) chloride hexahydrate (NiCl$_2$·6H$_2$O) and hexamethyle-netetramine (C$_6$H$_{12}$N$_4$; HMTA) were purchased from, HiMedia. Vanadium trichloride (VCl$_3$) was procured from Sigma Aldrich. Sulphuric acid (H$_2$SO$_4$), ethanol and acetone were acquired from S.D. Fine-Chem Ltd. The 5 wt% Nafion solution was purchased from Alfa Aesar. Double distilled water (DDW) was used to prepare all reaction solutions and electrolytes.

2.2 Preparation of gCN and S-gCN

Both pristine and S-doped gCN were prepared *via* the thermal polycondensation of precursor-modified melamine.[36] In a typical experiment, 3 g each of melamine and urea were mixed thoroughly using a mortar and pestle, before being transferred to a crucible and heated in a furnace at 550 °C for 3 h. After cooling to room temperature naturally, the obtained yellow powder was pounded into a fine powder to obtain gCN. For the synthesis of S-gCN, the same procedure was carried out, but 3 g of thiourea was used instead of urea for 1% doping of sulphur.[37]
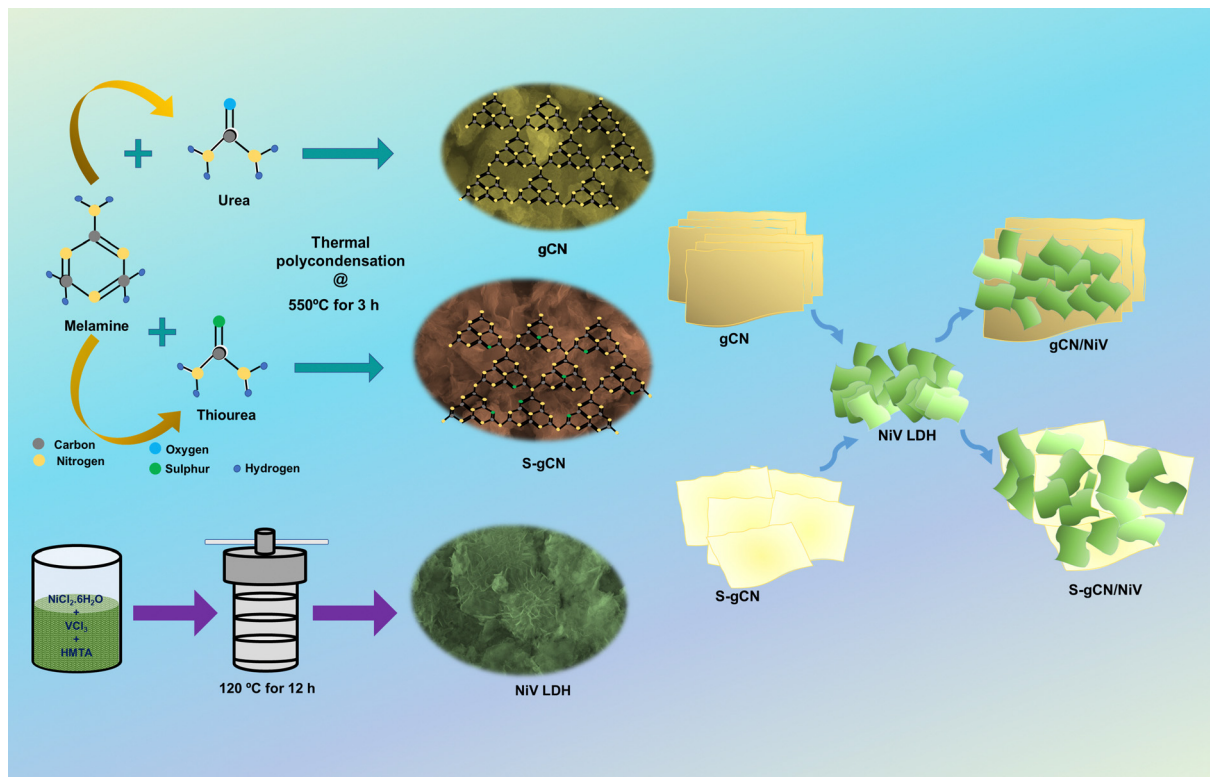
2.3 Preparation of NiV LDH

NiV LDH was prepared using a facile hydrothermal approach.[38] In the procedure, 2.6 mmol of NiCl$_2$·6H$_2$O, 0.64 mmol of VCl$_3$ and 6.48 mmol of HMTA were dissolved in 50 mL DDW. After stirring for 20 min, the solution was transferred into an 80 mL stainless autoclave with a Teflon lining and heated at 120 °C for 12 h. After cooling to room temperature, the obtained product was washed by centrifuging with DDW, 3 times and with ethanol, 2 times. The NiV LDH powder was obtained by drying the washed powder at 60 °C for 12 h.

2.4 Preparation of gCN/NiV and S-gCN/NiV composites

The NiV LDH-modified S-gCN (S-gCN/NiV) composite was prepared *via* simple ultrasonic mixing of equal weights of NiV LDH and S-gCN. In a typical procedure, 100 mg of both S-gCN and NiV LDH were mixed in DDW in a closed vial and sonicated for 12 h in an ice bath. After sonication, the sample was washed in ethanol and dried in a hot air oven for 12 h at 60 °C. The undoped gCN/NiV composite was prepared using the same

Scheme 1 Schematic representation of the preparation of doped and undoped g-C_3N_4/NiV LDH composites.

procedure as above but using gCN instead of S-gCN. The preparation of the discussed samples is depicted in Scheme 1.

2.5 Material characterization

The crystallographic properties were characterized *via* X-ray diffraction (XRD) analysis (Rigaku Ultima IV) using Cu Kα radiation of wavelength 1.5406 Å. An FEI Quanta-250 FEG field emission scanning electron microscope (FE-SEM) was used to analyse the morphology of the samples, and energy dispersive X-ray analysis (EDAX) with FESEM was used to obtain the compositional information. The specific surface area of the prepared materials was analysed using Brunner–Emmett–Teller (BET) analysis (Microtrac, BELSORP-max). The surface-level compositional information and chemical states were examined *via* X-ray photoelectron spectroscopy (XPS) (PHI 5000C Probe III, Japan).

2.6 Working electrode preparation

The prepared sample (3 mg) was sonicated in a 1 ml mixture of ethanol, DDW and 5 wt% Nafion solution (8 : 1.5 : 0.5) for 30 min to form a homogenous catalyst ink. A well-cleaned and polished glassy carbon electrode (GCE) was coated with 5 μL of the catalyst ink and allowed to dry at 40 °C for 10 min. The catalyst loading on the GCE with a diameter of 3 mm was calculated to be 0.015 mg cm^{-2}.

2.7 Electrochemical measurements

All electrochemical studies were carried out using a PARSTAT PMC-1000 potentiostat (Princeton Applied Research, Ametek

Scientific Instruments) in a three-electrode configuration where the catalyst-modified GCE served as the working electrode. A saturated calomel electrode (SCE) and a Pt mesh were used as the reference and counter electrodes, respectively, in 0.5 M H_2SO_4 of pH 0. The prepared samples were subjected to linear sweep voltammetry (LSV) polarization studies in the potential range of 0 to −1 V *vs.* SCE at 5 mV s^{-1}. Before this, the catalyst had been stabilized by recording cyclic voltammetry (CV) curves for 100 cycles in the potential window of 0 to −1 V *vs.* SCE. Electrochemical impedance spectroscopy (EIS) measurements were carried out from 100 kHz to 100 mHz at an HER overpotential of −0.8 V *vs.* RHE. Electrochemical surface area (ECSA) analysis was carried out by recording cyclic voltammograms in the non-faradaic region of −0.36 to −0.16 V *vs.* RHE at various scan rates from 10 to 200 mV s^{-1}. The durability of the catalyst electrode was analyzed through chronopotentiometry at 10 mA cm^{-2} for 8 h. The measured potential was converted in terms of the RHE using the formula $E_{RHE} = E_{SCE} + E°_{SCE} + 0.059 \times pH$, where $E°_{SCE}$ is 0.2412 V. All LSV polarization curves were *iR* drop compensated.

3. Results and discussion

The crystallographic structural properties of the prepared samples were studied using XRD analysis, and the diffractogram is given in Fig. 1. For gCN, the strong peak at 27.5° is due to the interplanar stacking of the (002) plane of the graphitic material, with an interplanar *d*-spacing of 0.32 nm. The smaller peak at
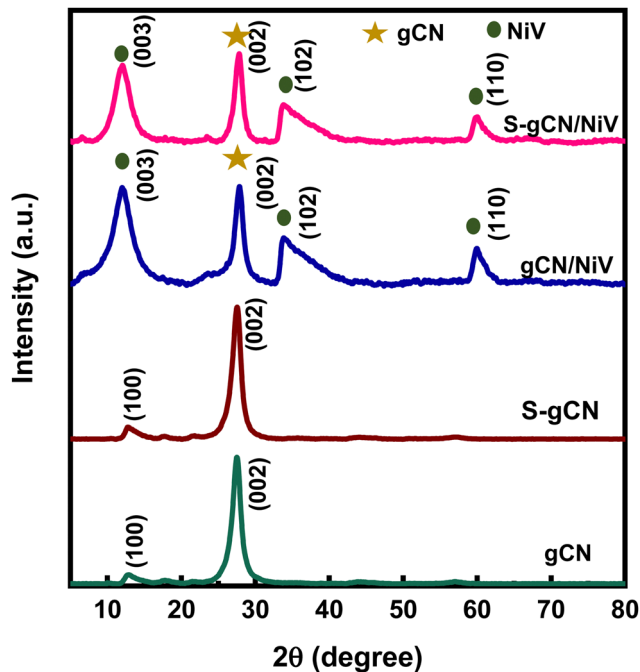
Fig. 1 X-ray diffractograms of the prepared samples.

$12.9°$ corresponds to the (100) plane of the interlayer structural packing, with a d-spacing of 0.69 nm. The diffraction pattern matches the standard pattern of g-C$_3$N$_4$ in the hexagonal phase (JCPDS 87-1526). S-gCN has the same structure as gCN, except that there is a mild shift in the 2θ value of the (100) plane to $12.7°$, which can be ascribed to a slight increase in the d spacing (0.7 nm) in the c-axis direction. The NiV LDH shows distinctive peaks at $11.8°$, $23.7°$, $33.9°$, $34.4°$ and $59.8°$, which are indexed to hkl planes (003), (006), (101), (012) and (110), respectively (Fig. S1, ESI†). The peaks in NiV match well with the reference nickel–vanadium carbonate hydroxide hydrate (JCPDS 052-1627). The peaks corresponding to the (101) plane at $33.9°$ and the (012) plane $34.4°$ combined to form a single distorted peak, as did the peaks of (110) at $59.9°$ and (113) at $60.3°$. gCN/NiV and S-gCN/NiV have a mixture of peaks from both gCN and NiV. The peaks of g-C$_3$N$_4$ are slightly left shifted whereas the peaks of NiV LDH are slightly right shifted, which corresponds to an increase and decrease in the interplanar spacing, respectively, suggesting a possible strain in the structure. The local strain in a material alters its surface electronic structures which directly affects the catalytic properties of a material.[39] In particular, compressive strain in a catalyst leads to a better interaction with the reaction intermediates, resulting in better HER activity.[40] The strain due to combining NiV LDH and S-gCN is thus speculated have a similar effect on the adsorbed hydrogen species for promoted hydrogen evolution, as can be seen from Table S1 (ESI†).

FE-SEM analysis was carried out to acquire the morphology of the prepared samples, and the images are presented in Fig. 2(a)–(d). gCN is composed of agglomerated layers (Fig. 2(a)), whereas the layers in S-gCN are more defined and crumpled (Fig. 2(b)). This also agrees with the increased

d-spacing of the interlayer packing for S-gCN when compared with gCN, as characterized by XRD. The modification of the precursor plays a crucial role in the resultant morphology of the samples.[16] g-C$_3$N$_4$ prepared *via* the usual route of polycondensation of melamine alone was composed of large particles of agglomerated layers that are greater than 3 μm in width (Fig. S2, ESI†). In contrast, modification of the precursor by mixing melamine with either urea or thiourea produced more specified layers. This will be beneficial for improving the surface area and exposing active sites for catalytic applications. The NiV LDH was composed of thin nanosheets bound into 3D spheres, as can be seen in Fig. S3 (ESI†). From Fig. 2(c), we can see that, in gCN/NiV, the gCN particles are covered with NiV LDH sheets, and from Fig. 2(d) it can be seen that the layers of S-gCN and NiV LDH have fused together forming a 2D/2D interface of the S-gCN/NiV microstructure. Sonication has collapsed the assembly of NiV LDH 3D spheres into single layers to form a well-fused layer microstructure with S-gCN. From EDAX analysis, the elemental composition of the samples was determined. The absence of any other impurity elements in the EDAX spectra (Fig. 2(e)–(h)) affirms the sample purity. The peak at 1.5 keV corresponds to Al and arises due to the signal from the aluminium stage used for mounting the samples. The EDAX maps of S-gCN and S-gCN/NiV are presented in Fig. 2(i) and (j), respectively, and those for gCN and gCN/NiV are presented, respectively, in Fig. S5 and S6 (ESI†), which show that the elements are distributed evenly throughout the samples. The atomic compositions of all the samples are presented in Fig. 2(k).

Furthermore, XPS analysis was carried out to obtain accurate information about chemical composition at the surface level and the oxidation state of S-gCN/NiV. The survey scan of S-gCN/NiV displays the presence of C, N, S, O, Ni and V, as given in Fig. S7 (ESI†). The core level spectrum of C 1s consists of two peaks at 284.85 and 288.17 eV, as shown in Fig. 3(a), corresponding to graphitic C=C bonding and N trigonally bonded to sp^2 carbon atoms (C–N–C).[41] The core level spectrum of N 1s is given in Fig. 3(b) and consists of two convoluted peaks at 398.6 and 400.6 eV that are corroborated to sp^2 hybridized N in C=N–C and sp^3 hybridized N in secondary amine ((C$_2$)–N–H) binding.[42] Since the quantity of sulphur is very low in the doped samples, the core spectrum of S 2p is noisy (Fig. 3(c)), also considering the fact that sulphur usually requires a longer acquisition time than other elements in XPS. However, curve fitting yields a distinctive peak at 163.5 eV, which corresponds to C–S bonding.[43] The core level spectrum of Ni 2p shown in Fig. 3(d) shows Ni two peaks at 856.47 eV and 874.19 eV that correspond to Ni 2p$_{3/2}$ and Ni 2p$_{1/2}$ with respective satellite peaks at 862.1 and 879.9 eV, denoting the spin–orbital splitting of the Ni 2p orbital. The difference between the peaks is ~17.1 eV, which is characteristic of Ni^{2+}.[44] Fig. 3(e) shows the core level peak of O 1s at 531.8 eV, which denotes M–OH bonding. The magnified core level spectrum of V 2p, as shown in Fig. 3(f), shows the spin–orbital splitting of V 2p$_{1/2}$ and V 2p$_{3/2}$ at 524.9 and 517.4 eV, respectively.[45,46] The V 2p$_{3/2}$ peak is further resolved into the V^{5+} peak at 517.4 eV and the V^{3+}
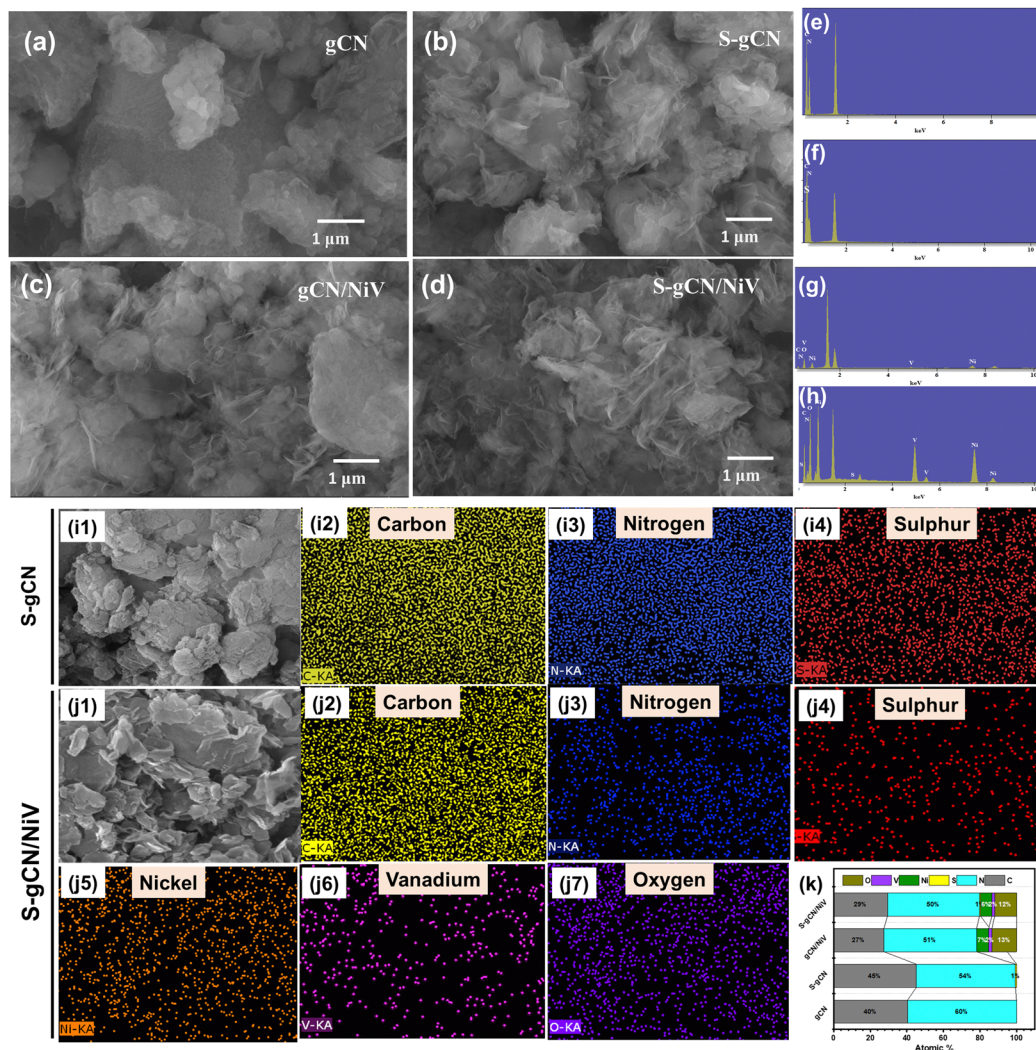
Fig. 2 FE-SEM images of the prepared samples (a)–(d). EDAX spectra of (e) gCN, (f) S-gCN, (g) gCN/NiV and (h) S-gCN/NiV; EDAX maps of (i1)–(i4) S-gCN and (j1)–(j7) S-gCN/NiV; and (k) atomic composition of all samples analysed *via* EDAX.

peak at 515.6 eV.[47] This indicates that V is mostly present in the +5 oxidization state, which is its most stable state, along with a partial oxidation +3 state.[45,48]

The effect of interfacing two 2D layered materials on the surface area of the composite was studied through BET analysis, and the respective pore size distributions were examined using the Barrett–Joyner–Halenda (BJH) technique. From Fig. 4, it is evident that all the prepared samples show a type IV isotherm of N_2 adsorption–desorption, which is the behaviour of mesoporous adsorbent structures. The type IV isotherm is accompanied by complete monolayer adsorption, with increased N_2 uptake with increasing P/P_0 due to multilayer adsorption.[49] The multilayer adsorption could also possibly arise due to the adsorption in multiple layers in layered structures of the prepared samples. Hence, the mono-multilayer adsorption of the prepared samples is confirmed using BET analysis. Table 1 lists the values obtained for the specific surface area, average pore size and total pore volume as computed using the BJH method. The surface area of the

gCN/NiV composite increased sharply, and S-gCN/NiV has the highest surface area among all the samples due to the intermingling of S-gCN and NiV layers. This enhancement in the surface area will positively influence the HER catalytic performance by revealing more active sites for the reaction.[50]

The HER catalysis behaviour of the prepared samples is illustrated by the LSV polarization curves recorded in 0.5 M H_2SO_4, at 5 mV s^{-1}, as shown in Fig. 5(a). Among all the samples, S-gCN/NiV showed the lowest onset potential of 465 mV, whereas gCN/NiV, S-gCN and gCN, respectively, showed 510, 493 and 586 mV. Similarly, S-gCN/NiV shows the lowest overpotential of 560 mV at 10 mA cm^{-2}, while those for gCN/NiV, S-gCN and gCN are, respectively, 606, 636 and 687 mV for the same current density. The lower overpotentials of gCN/NiV and S-gCN/NiV compared with gCN and S-gCN show that forming composites between g-C_3N_4 and the NiV LDH significantly improves the HER catalytic activity. This is because, the NiV LDH imparts its intrinsic metallic catalytic activity to g-C_3N_4 for a boosted HER process.[51] Moreover, the lower
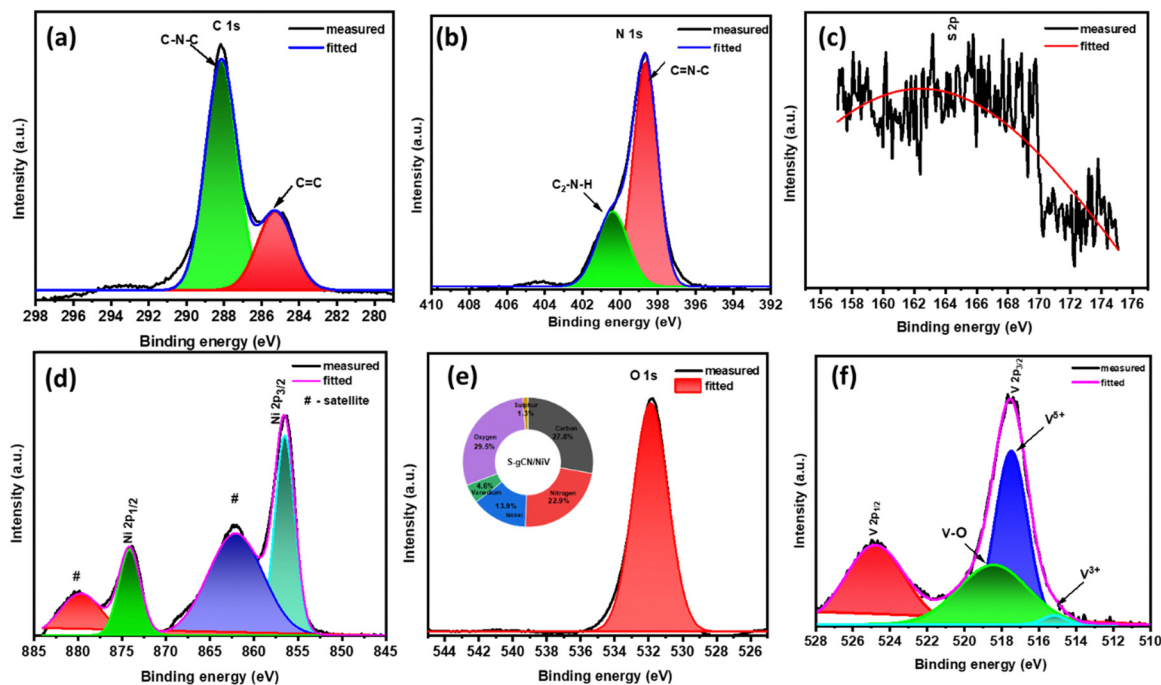
Fig. 3 XPS core level spectra of (a) C 1s, (b) N 1s, (c) S 2p, (d) Ni 2p, (e) O 1s and V 2p and (f) zoomed V 2p for S–gCN/NiV. The elemental composition data acquired from XPS are given as the inset in (e).

overpotential value of S-gCN/NiV than gCN/NiV and that of S-gCN compared with gCN implies that S doping imparts an influence to improve HER catalysis. This arises mainly from the substitutional defects created on the structure of g-C$_3$N$_4$ due to S doping, where doping sites act as catalytic centres.[52,53]

To further elucidate the efficiency of the prepared composite, the best-performing sample, i.e., S-gCN/NiV, was coated onto an FTO substrate (1 × 1 cm) and exposed to xenon lamp irradiation (100 mW cm^{-2}) with a UV filter and linear sweep voltammograms recorded in the same potential window of 0 to −1 V vs. RHE, in 0.5 M H$_2$SO$_4$. Fig. S12 in the ESI† shows the LSV profiles recorded under dark and illuminated conditions, where it can be seen that the irradiated sample shows a potential of 295 mV at 10 mA cm^{-2}, whereas without irradiation the same sample shows a potential of 526 mV at the same current density. Hence, S-gCN/NiV shows more promise as a photoelectrode for the HER, which remains to be explored. Table S2 in the ESI,† compares g-C$_3$N$_4$-and-LDH-based composites for the electrochemical HER, and it can be seen that the S-gCN/NiV composite shows a comparable performance with its binary-composite counterparts.

The intrinsic catalytic activity of a material can be revealed via Tafel analysis. The Tafel equation relates the current density j, to the overpotential value η, as η = b log |j| + a. Thus, a plot between log |j| and η will be linear with a slope b, which is known as the Tafel slope. Theoretical Tafel slope values of 120, 40 and 30 mV dec^{-1} are assigned correspondingly to the Volmer, Heyrovský and Tafel steps.[54] Hence, Tafel slope analysis can provide insight into the catalyst's natural catalytic activity and elucidate the catalytic reaction's rate-determining

step. Tafel plots of the studied catalysts are shown in Fig. 5(b). gCN and S-gCN, with Tafel slope values of 126 and 110 mV dec^{-1}, respectively, indicate that the Volmer reaction is the rate-limiting step, i.e., there is excessive adsorption of solvated H$^+$ onto the catalyst surface, but deficient desorption or recombination of adsorbed H* into H$_2$, which hinders the HER. The lower Tafel slope values of gCN/NiV (90 mV dec^{-1}) and S-gCN/NiV (79 mV dec^{-1}) show that the adsorbed H* are generously converted into H$_2$. This suggests that gCN and S-gCN act as strong adsorbing sites for H* and deter their recombination and desorption into H$_2$. The infused NiV LDH sheets may break down the H* adsorption in gCN or S-gCN and facilitate H$_2$ evolution, most probably through the Heyrovský step, which is the electrochemical desorption step.[55] The mechanism of hydrogen evolution in gCN and S-gCN/NiV is depicted in Scheme 2.

The electrochemical impedance spectra of the prepared samples are given in Fig. 6(a), where all the samples show depressed semi-circles and the equivalent circuit is given as the inset. The values in the x-axis at the beginning and end of the semicircle, respectively, denote, R_u and $R_u + R_{ct}$, where R_u is the uncompensated resistance arising due to solution resistance and electrical contacts, and R_{ct} is the charge transfer resistance. g-CN and S-gCN exhibit large semicircles, with R_{ct} values of 542 and 367 Ω, respectively. Both gCN/NiV and S-gCN/NiV show diminished semicircles with significantly decreased R_{ct} values of 95 and 36 Ω, respectively. Thus, combining NiV LDH with g-C$_3$N$_4$ boosts the kinetics of charge transfer for the HER reaction.[56] The smaller R_{ct} value of S-gCN in comparison with gCN and of S-gCN/NiV compared with that of gCN/NiV
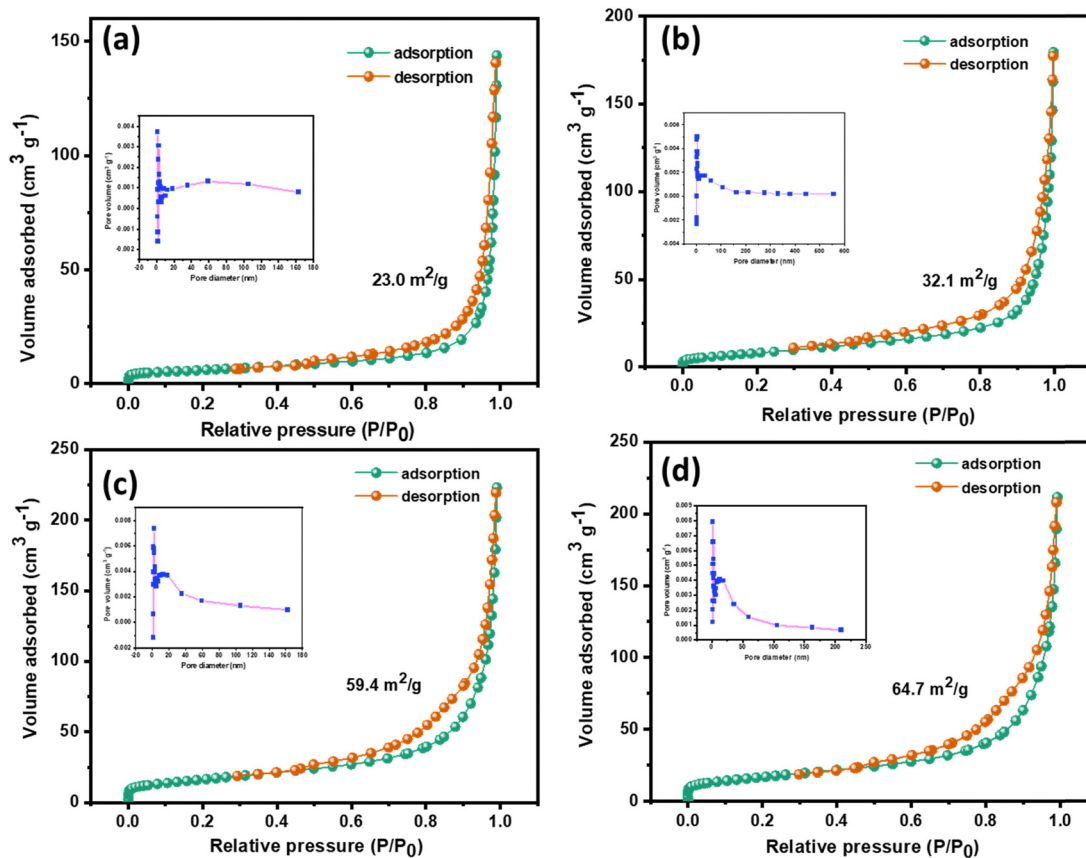
Fig. 4 Nitrogen adsorption–desorption isotherms of (a) gCN, (b) S-gCN, (c) gCN/NiV and (d) S-gCN/NiV. The corresponding BJH pore size distribution plot is given as an inset in each figure.

Table 1 Comparison of the morphology, specific surface area, average pore size and total pore volume of the prepared samples

Sample	Morphology	Specific surface area ($m^2 g^{-1}$)	Average pore size (nm)	Total pore volume ($cm^3 g^{-1}$)
gCN	Layers agglomerated into microparticles	23.0	36.1	0.2074
S-gCN	Layered microstructure	32.1	30.0	0.1846
gCN/NiV	NiV LDH layers covering the surface of gCN particles	59.4	21.7	0.3233
S-gCN/NiV	NiV and S-gCN layers fused together	64.7	19.2	0.2975

suggests that S doping imparts better kinetics for the exchange of electrons, possibly because the doping defect sites act as catalytic centres.[53] Moreover, S doping also changes the band structure and band gap of g-C_3N_4, and from Fig. S8 (ESI†) it can also be seen that S-gCN has a slightly lower band gap than undoped gCN. Since the composite was prepared *via* external sonication mixing of gCN or S-gCN and NiV, it did not alter the band gap of g-C_3N_4 to a notable extent; rather, *in situ* reactions for preparing the composites may have effected modification of the band structures. The activity parameters of R_{ct}, η and the Tafel slope for the prepared catalysts are compared in Fig. 6(b).

The electrochemical surface area (ECSA) denotes the surface of the catalyst that is available for the electrochemical reaction and is an important parameter to endorse the catalytic activity. A larger ECSA value corresponds to a greater catalytic activity.

The ECSA is usually obtained by determining the double-layer capacitance (C_{dl}).[57] To obtain the C_{dl} value, CV curves were recorded at various scan rates ranging from 10 to 200 mV s^{-1} in the non-faradaic potential region of −0.3 to −0.1 V *vs.* RHE, where the current is diffusion limited. The CV curves in the non-faradaic region at different scan rates (in mV s^{-1}) for S-gCN/NiV are given in Fig. 7(a), and those for the remaining samples are given in Fig. S9–S11 (ESI†). The difference between the anodic and cathodic peak current at −0.2 V *vs.* RHE is plotted against the scan rate to yield a linear graph as shown in Fig. 7(b). The slope of the line represents $2C_{dl}$, from which C_{dl} and thus the ECSA can be determined using the following relation: ECSA = C_{dl}/C_s, where C_s is the specific capacitance of a planar smooth surface. There exist inconsistencies in the literature with values of C_s, and this often results in
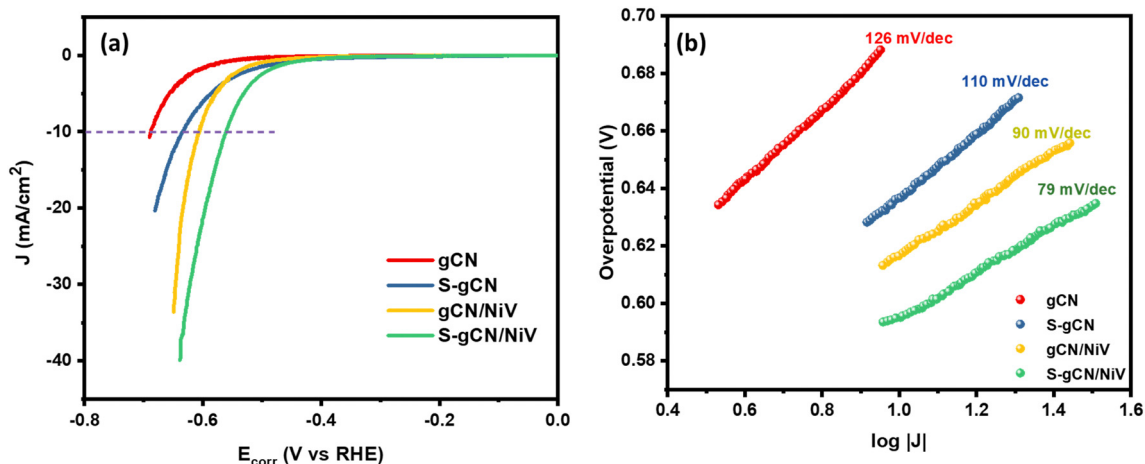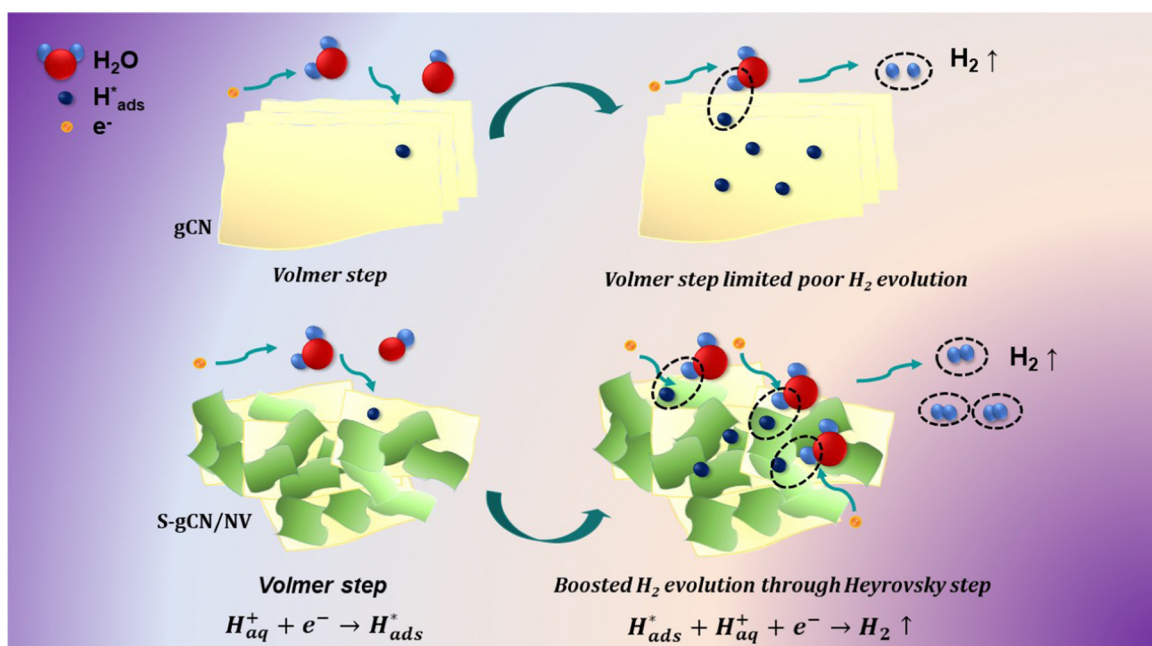
Fig. 5 (a) LSV polarization curves and (b) Tafel plot of the prepared samples.

Scheme 2 Schematic representation of the HER mechanism in gCN and S-gCN/NiV samples.

exaggeration or understatement of the real ECSA value.[58] However, since C_s is a constant, the C_{dl} value can be taken as a direct indicator of the ECSA. S-gCN/NiV showed the highest C_{dl} value of 244 µF cm^{-2}, followed by gCN/NiV, S-gCN and gCN at 159 µF cm^{-2}, 96 µF cm^{-2} and 90 µF cm^{-2}, correspondingly. The profound increase in ECSA for the composites when compared with the sole material is due to the interfacing of NiV layers with g-C$_3$N$_4$, which results in a high specific surface area, as also verified by the BET analysis data.

The stability of S-gCN/NiV for sustained HER operation was investigated using chronopotentiometry (CP). Since a GCE is not suitable for prolonged studies, 200 µl of the catalyst ink was coated onto a stainless steel (SS) foil of area 1 × 1 cm, and this S-gCN/NiV-modified SS (S-gCN/NiV@SS) was used as the working electrode. LSV of the bare SS and S-gCN/NiV@SS electrodes was carried out before CP measurements were obtained, after which CP was performed at −100 mA cm^{-2} for 30 000 s (Fig. 7(c)); from this, it can be seen that S-gCN/NiV@SS has a stable catalytic performance. As shown in Fig. 7(d), the S-gCN/NiV@SS electrode remained intact and showed negligible variance between the LSV curves recorded before after the chronopotentiometric study of nearly 8 h.

The structural stability of S-gCN/NiV was studied further by performing post-electrochemical XRD and FE-SEM analyses. The catalyst was scraped off the SS substrate after 8 h of chronopotentiometry and rinsed with DD water *via* centrifugation. For XRD analysis, the sample was mixed with 8 mg of amorphous glass powder, whose XRD signal was used as the
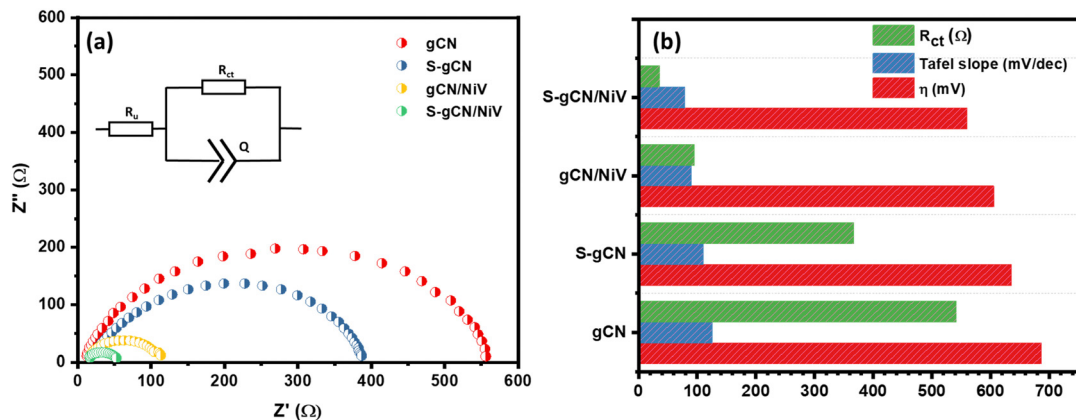
Fig. 6 (a) EIS Nyquist plots and (b) comparison of activity parameters of the studied catalysts.
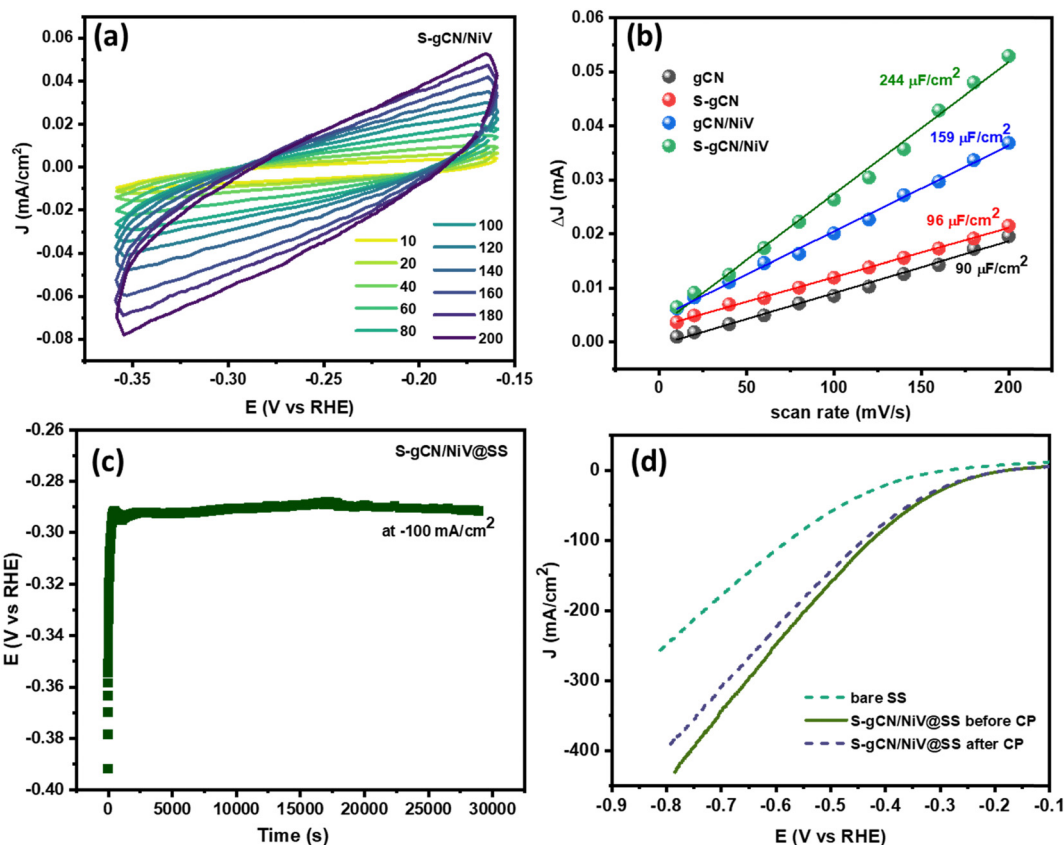

Fig. 7 (a) CV curves measured at different scan rates in the non-faradaic region for S-gCN/NiV. (b) Plot of the double layer charging current density *vs.* scan rate to illustrate C_{dl}. (c) Chronopotentiometric analysis of S-gCN/NiV coated on SS at −100 mA cm^{-2} for ∼8 h. (d) LSV curves of S-gCN/NiV@SS recorded before and after chronopotentiometry; the curve of bare SS is shown for comparison.

background, to obtain the exact pattern of the sample, and the scanning rate was lowered to 0.5° min^{-1}. This change to the scan rate was carried out to compensate for the limited quantity of the catalyst sample, since it is a recommended practice not to overload catalyst for any catalysis. For FE-SEM analysis, the scraped and washed catalyst was used as such. Fig. 8(a) shows that in the XRD pattern of the post-CP sample, there is a

decrease in the intensity of the peak that corresponds to the (003) plane of NiV LDH. Moreover, the peaks corresponding to the (101) and (012) planes of NiV LDH have broadened. This shows that S-gCN/NiV almost retains its structure, but NiV LDH is prone to a moderate structural deformation. This is also verified from the FE-SEM images shown in Fig. 8(b) and (c), where it can be seen that S-gCN/NiV retains its layered structure
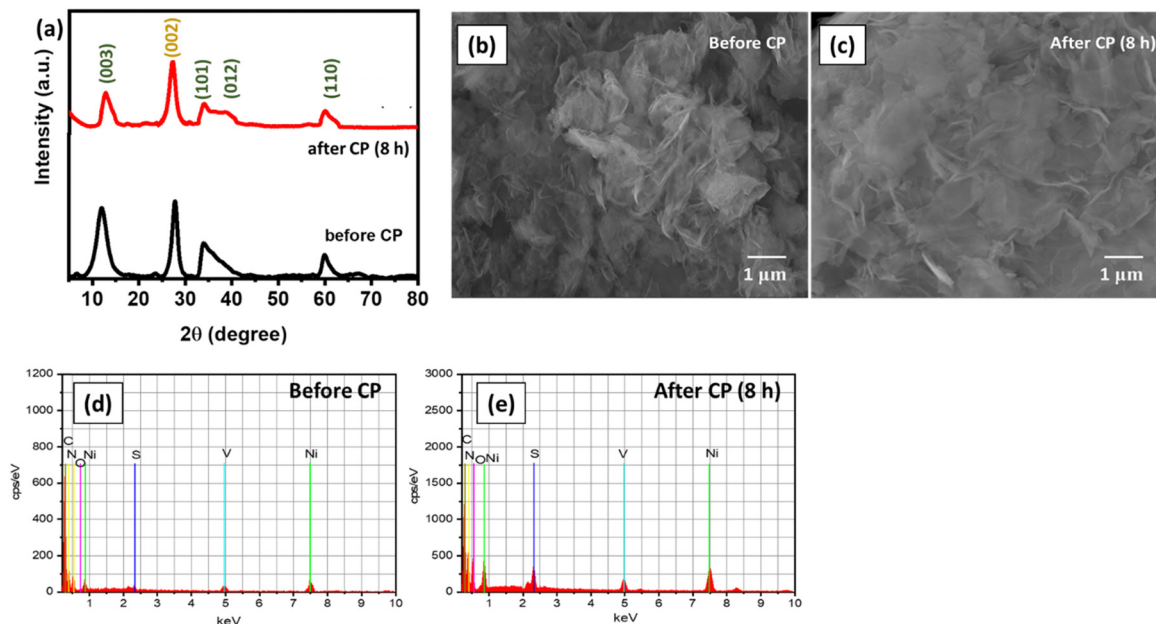
Fig. 8 (a) XRD pattern of S-gCN/NiV before and after CP; FE-SEM images of S-gCN/NiV (b) before and (c) after CP; and EDAX analysis of S-gCN/NiV (d) before and (e) after CP.

Table 2 Compositional information for S-gCN/NiV obtained from EDAX analysis of the samples before and after CP

Element	Atomic composition (%)	
	Before CP	After CP (8 h)
Ni	5.55	5.67
V	2.17	1.82
O	13.82	14.30
C	43.63	40.15
N	33.82	36.09
S	1.01	1.97
Total	100	100

post-catalysis, although the layers are denser and more stacked after the CP analysis. EDAX analysis revealed that the elemental composition of the catalyst does not vary significantly, except for vanadium, which is ∼16% lower in the post-catalysis samples, as can be seen from Fig. 8(d), (e) and Table 2. This could be due to the harsh acidic conditions under which the HER is performed. The amount of sulphur in the post-CP sample is much higher, due to the penetration of sulphate ions from the electrolyte. These studies reveal that S-gCN/NiV possesses considerable structural and morphological stability after 8 hours of HER catalysis.

4. Conclusion

Novel composites of bare and S-doped g-C_3N_4 with the NiV LDH were prepared and their electrochemical HER catalysis performance was studied. The layered microstructure of the composites was confirmed via FE-SEM analysis and, in comparison with the unadorned gCN and S-gCN samples, a significant improvement in the specific surface area of their composites with the NiV LDH was verified through BET analysis.

Electrochemical polarization studies showed that the composites demonstrated an increased catalytic activity. Tafel analysis implies that the infusion of NiV LDH layers with g-C_3N_4 drives the HER by Volmer–Heyrovský mechanism, whereas in plain gCN and S-gCN, the HER is limited by the Volmer step. Doping with sulfur also positively impacts the HER catalysis, mainly through the exposure of more active sites, as both S-gCN/NiV and S-gCN showed better catalytic activity than the undoped gCN/NiV and gCN, respectively. Among the prepared catalysts, S-gCN/NiV showed a lower overpotential of 560 mV at 10 mA cm^{-2} and a Tafel slope of 79 mV dec^{-1}, and exhibited profound stability under continuous catalysis for ∼8 h. This study proposes that the poor intrinsic catalytic activity of g-C_3N_4 for the HER can be overcome via heteroatom doping and the formation of composites with LDHs, which paves the way for further photoelectrochemical HER and water-splitting studies.

Author contributions

G. Srividhya: conceptualization, data curation, investigation, methodology, visualization and writing; N. Ponpandian: conceptualization, resources, funding acquisition and validation.

Conflicts of interest

There are no conflicts of interest to declare.

Acknowledgements

References

1 M. A. Rosen and S. Koohi-Fayegh, *Energy Ecol. Environ.*, 2016, **1**, 10–29.

2 P. Zhao, W. Xu, A. Liu, W. Wu, J. Wang and X. Wang, *Int. J. Hydrogen Energy*, 2023, **48**, 9198–9218.

3 S. Y. Tee, K. Y. Win, W. S. Teo, L.-D. Koh, S. Liu, C. P. Teng and M.-Y. Han, *Adv. Sci.*, 2017, **4**, 1600337.

4 S. Singla, S. Sharma, S. Basu, N. P. Shetti and T. M. Aminabhavi, *Int. J. Hydrogen Energy*, 2021, **46**, 33696–33717.

5 L. Tian, Z. Li, X. Xu and C. Zhang, *J. Mater. Chem. A*, 2021, **9**, 13459–13470.

6 A. Manikandan, P. R. Ilango, C.-W. Chen, Y.-C. Wang, Y.-C. Shih, L. Lee, Z. M. Wang, H. Ko and Y.-L. Chueh, *J. Mater. Chem. A*, 2018, **6**, 15320–15329.

7 P. R. Ilango, H. Huang, L. Li, S. Yang and S. Peng, *Solid State Sci.*, 2021, **117**, 106627.

8 D. Yu, P. R. Ilango, S. Han, M. Ye, Y. Hu, L. Li and S. Peng., *Int. J. Hydrogen Energy*, 2019, **44**, 32054–32065.

9 Z. Cai, Z. Wang, Y. Xia, H. Lim, W. Zhou, A. Taniguchi, M. Ohtani, K. Kobiro, T. Fujita and Y. Yamauchi, *Angew. Chem.*, 2021, **133**, 4797–4805.

10 H. Wu, C. Feng, L. Zhang, J. Zhang and D. P. Wilkinson, *Electrochem. Energy Rev.*, 2021, **4**, 473–507.

11 A. Lasia, *J. Hydrogen Energy*, 2019, **44**, 19484–19518.

12 J. Mei, T. He, J. Bai, D. Qi, A. Du, T. Liao, G. A. Ayoko, Y. Yamauchi, L. Sun and Z. Sun, *Adv. Mater.*, 2021, **33**, 2104638.

13 H. Q. Fu, M. Zhou, P. F. Liu, P. Liu, H. Yin, K. Z. Sun, H. G. Yang, M. Al-Mamun, P. Hu, H.-F. Wang and H. Zhao, *J. Am. Chem. Soc.*, 2022, **144**, 6028–6039.

14 S. Geng, W. Yang and Y. S. Yu, *J. Catal.*, 2019, **375**, 441–447.

15 T. Li, J. Wu, L. Qiao, Q. Zhu, Z. Fu, J. Lin, J. Chen, L. Peng, B. Wang and Z. Chen, *Mater. Today Energy*, 2022, **26**, 101002.

16 X. Chen, R. Shi, Q. Chen, Z. Zhang, W. Jiang, Y. Zhu and T. Zhang, *Nano Energy*, 2019, **59**, 644–650.

17 H. Wang, X. Li and J. Yang, *ChemPhysChem*, 2016, **17**, 2100–2104.

18 Sk Riyajuddin, S. K. Tarik Aziz, S. Kumar, G. D. Nessim and K. Ghosh, *ChemCatChem*, 2020, **12**, 1394–1402.

19 X. She, J. Wu, H. Xu, J. Zhong, Y. Wang, Y. Song, K. Nie, Y. Liu, Y. Yang, M.-T. F. Rodrigues, R. Vajtai, J. Lou, D. Du, H. Li and P. M. Ajayan, *Adv. Energy Mater.*, 2017, **7**, 1700025.

20 Z.-A. Lan, G. Zhang and X. Wang, *Appl. Catal., B*, 2016, **192**, 116–125.

21 Y.-P. Zhu, T.-Z. Ren and Z.-Y. Yuan, *ACS Appl. Mater. Interfaces*, 2015, **7**, 16850–16856.

22 J. Jiang, Z. Xiong, H. Wang, G. Liao, S. Bai, J. Zou, P. Wu, P. Zhang and X. Li, *J. Mater. Sci. Technol.*, 2022, **118**, 15–24.

23 M.-H. Vu, M. Sakar, C.-C. Nguyen and T.-O. Do, *ACS Sustainable Chem. Eng.*, 2018, **6**, 4194–4203.

24 L. Bai, H. Huang, S. Yu, D. Zhang, H. Huang and Y. Zhang, *J. Energy Chem.*, 2022, **64**, 214–235.

25 H. Zhao, H. Zhang, G. Cui, Y. Dong, G. Wang, P. Jiang, X. Wu and N. Zhao, *Appl. Catal., B*, 2018, **225**, 284–290.

26 H. Boumeriame, E. S. Da Silva, A. S. Cherevan, T. Chafik, J. L. Faria and D. Eder, *J. Energy Chem.*, 2022, **64**, 406–431.

27 L. Lv, Z. Yang, K. Chen, C. Wang and Y. Xiong, *Adv. Energy Mater.*, 2019, **9**, 1803358.

28 Z.-Y. Zhang, H. Tian, L. Bian, S.-Z. Liu, Y. Liu and Z.-L. Wang, *J. Energy Chem.*, 2023, **83**, 90–97.

29 M. Luo, J. Yang, X. Li, M. Eguchi, Y. Yamauchi and Z.-L. Wang, *Chem. Sci.*, 2023, **14**, 3400–3414.

30 L. Feng, Y. Du, J. Huang, L. Cao, L. Feng, Y. Feng, Q. Liu, D. Yang and K. Kajiyoshi, Sustain, *Energy Fuels*, 2020, **4**, 2850–2858.

31 P. M. Bodhankar, P. B. Sarawade, G. Singh, A. Vinu and D. S. Dhawale, *J. Mater. Chem. A*, 2021, **9**, 3180–3208.

32 D. He, L. Cao, J. Huang, K. Kajiyoshi, J. Wu, C. Wang, Q. Liu, D. Yang and L. Feng, *J. Energy Chem.*, 2020, **47**, 263–271.

33 M. Shakeel, M. Arif, G. Yasin, B. Li and H. D. Khan, *Appl. Catal., B*, 2019, **242**, 485–498.

34 M. Arif, G. Yasin, M. Shakeel, X. Fang, R. Gao, S. Ji and D. Yan, *Chem. – Asian J.*, 2018, **13**, 1045–1052.

35 B. Zhang, J. Li, Q. Song and H. Liu, *Int. J. Energy Res.*, 2022, **46**, 12406–12416.

36 N. Tian, Y. Zhang, X. Li, K. Xiao, X. Du, F. Dong, G. I. N. Waterhouse, T. Zhang and H. Huang, *Nano Energy*, 2017, **38**, 72–81.

37 L. Ye and S. Chen, *Appl. Surf. Sci.*, 2016, **389**, 1076–1083.

38 A. Tyagi, M. C. Joshi, A. Shah, V. K. Thakur and R. K. Gupta, *ACS Omega*, 2019, **4**, 3257–3267.

39 X. Wang, Y. Zhu, A. Vasileff, Y. Jiao, S. Chen, L. Song, B. Zheng, Y. Zheng and S.-Z. Qiao, *ACS Energy Lett.*, 2018, **3**, 1198–1204.

40 S. Wang, L. Wang, L. Xie, W. Zhao, X. Liu, Z. Zhuang, Y. Zhuang, J. Chen, S. Liu and Q. Zhao, *Nano Res.*, 2022, **15**, 4996–5003.

41 F. Qiao, J. Wang, S. Ai and L. Li, *Sens. Actuators, B*, 2015, **216**, 418–427.

42 P. Liu, N. Sun, Y. Liang and F. Chen, *Res. Chem. Intermed.*, 2018, **44**, 843–857.

43 A. Kadam, Md Moniruzzaman and S.-W. Lee, *Molecules*, 2019, **24**, 450.

44 K. Fan, H. Chen, Y. Ji, H. Huang, P. M. Claesson, Q. Daniel, B. Philippe, H. Rensmo, F. Li, Y. Luo and L. Sun, *Nat. Commun.*, 2016, **7**, 11981.

45 A. Karmakar, K. Karthick, S. S. Sankar, S. Kumaravel, R. Madhu, K. Bera, H. N. Dhandapani, S. Nagappan, P. Murugan and S. Kundu, *J. Mater. Chem. A*, 2022, **10**, 3618–3632.

46 D. Xiong, W. Li and L. Liu, *Chem. – Asian J.*, 2017, **12**, 543–551.

47 E. Hryha, E. Rutqvist and L. Nyborg, *Surf. Interface Anal.*, 2012, **44**, 1022–1025.

48 D. He, L. Cao, J. Huang, K. Kajiyoshi, J. Wu, C. Wang, Q. Liu, D. Yang and L. Feng, *J. Energy Chem.*, 2020, **47**, 263–271.

49 F. J. Sotomayor, K. A. Cychosz and M. Thommes, *Characterization of Micro/Mesoporous Materials by Physisorption: Concepts and Case Studies*, 2018, vol. 3.

50 H.-Y. Wang, Y.-Y. Hsu, R. Chen, T.-S. Chan, H. M. Chen and B. Liu, *Adv. Energy Mater.*, 2015, **5**, 1500091.

51 Y. Xu, K. Fan, Y. Zou, H. Fu, M. Dong, Y. Dou, Y. Wang, S. Chen, H. Yin, M. Al-Mamun, P. Liu and H. Zhao, *Nanoscale*, 2021, **13**, 20324–20353.

52 Y.-C. Chu, T.-J. Lin, Y.-R. Lin, W.-L. Chiu, B.-S. Nguyen and C. Hu, *Carbon N. Y.*, 2020, **169**, 338–348.

53 Y. Wang, Y. Tian, L. Yan and Z. Su, *J. Phys. Chem. C*, 2018, **122**, 7712–7719.

54 B. V. Tilak and C.-P. Chen, *J. Appl. Electrochem.*, 1993, **23**, 631–640.

55 G. Zhao, K. Rui, S. X. Dou and W. Sun, *Adv. Funct. Mater.*, 2018, **28**, 1803291.

56 D. Wang, Q. Li, C. Han, Q. Lu, Z. Xing and X. Yang, *Nat. Commun.*, 2019, **10**, 3899.

57 Y. Jiang, D. Zhong, L. Wang, J. Li, G. Hao, J. Li and Q. Zhao, *Chem. – Asian J.*, 2022, **17**, e202200380.

58 P. Connor, J. Schuch, B. Kaiser and W. Jaegermann, *Z. Phys. Chem.*, 2020, **234**, 979–994.